Extrinsic Trochoidal Dichroism is Modulated by Nanoparticle Symmetry

Lauren A. McCarthy,[1] Seyyed Ali Hosseini Jebeli,[2] Stephan Link[1,2,]*

AFFILIATIONS:

[1] Department of Chemistry, Rice University, 6100 Main Street, MS 60, Houston, Texas 77005, United States.

[2] Department of Electrical and Computer Engineering, Rice University, 6100 Main Street, MS 366, Houston, Texas 77005, United States.

*Corresponding Author: slink@rice.edu; (713) 348-4561

KEYWORDS: evanescent field polarization, trochoidal polarization, hybridized plasmons, nanoparticle symmetry

ABSTRACT:

The polarization properties of near-field confined light significantly diverge from their freely propagating counterparts. Polarized evanescent waves can support cycloid-like trochoidal field motion, generated by transverse oscillations that are out-of-phase with longitudinal oscillations, which are absent from free-space light. We have recently observed that trochoidal waves with opposite rotational directions preferentially excite hybridized plasmon modes in gold nanoparticle dimers (*Proc. Natl. Acad. Sci. U. S. A.* **2020,** *117*, 16143-16148). However, the symmetry properties responsible for this effect, named trochoidal dichroism, have not been investigated. Here, we lithographically fabricate nanoparticle assemblies with varying symmetry to uncover the geometric parameters driving sensitivity to trochoidal polarizations. We find that while symmetric structures, such as single nanorods, do not exhibit trochoidal dichroism, asymmetric nanoparticle arrangements facilitating a planar rotation of dipole orientations, with one or fewer planes of mirror symmetry, are trochoidal-active. In particular, fan-shaped nanorod assemblies tracing out the arch of the trochoidal field exhibit polarization-selective promotion of their bonding and antibonding hybridized plasmons. By characterizing trochoidal dichroism as a function of nanoparticle symmetry, we gain a deeper understanding of efficient nanoantenna design principles and molecular geometries that can be probed using this novel light-matter interaction.

Introduction:

Optical dichroisms efficiently probe molecular geometric properties. Widely utilized techniques, such as linear dichroism (LD) and circular dichroism (CD) couple to linear and helical charge motion, respectively, and measure the differential extinction of orthogonal light polarizations by the analyte.[1-2] While LD tracks alignment and orientation in anisotropic media, CD identifies chirality, or handedness, which dictates crucial aspects of molecular interactions with their surroundings. Recently, these molecular concepts have been extended to study the polarized light-matter interactions of plasmonic nanostructures.[3-7] The optical properties of noble metal nanoparticles are dominated by their plasmon resonance, which is the coherent oscillation of conduction band electrons.[8] Due to their close size-match with the wavelengths of exciting light, nanoparticle plasmons often exhibit CD that is orders of magnitude larger than that of their molecular counterparts.[9-10] Plasmonic structures, therefore, form attractive platforms as nanoscale waveplates, on-chip polarization-sensitive antennas,[11] and reporters of chiral signals from molecular templates.[12] Plasmonic assemblies have also been demonstrated to amplify and transduce the CD of nearby molecules to the plasmon resonance through near-field multipole interactions.[13] Further, polarization-dependent scattering is readily observable on the single nanoparticle level,[14-17] enabling characterization of heterogeneity amongst ensemble populations,[18-21] and deepening our understanding of the origin of dichroism in nanomaterials.[21]

LD and CD effectively characterize anisotropy and handedness, but there are additional forms of light polarization that remain underutilized,[22-24] thereby limiting the geometric information that is probable through optical means. While interference fields[25] and nanoscale-confined light[26-27] efficiently enhance CD, there is a need for novel dichroisms utilizing polarizations that can couple to electronic transitions to which traditional techniques are not

sensitive.[23] Trochoidal polarizations, for example, are found in laterally confined light[28-30] and feature field motion that is both planar and rotational,[28] producing a cycloidal, or cartwheeling wave motion as the light propagates forward.[31] Trochoidal dichroism (TD) is the differential extinction of orthogonal trochoidal polarizations by a material[24] and is expected to probe cycloidal charge motion in molecules, complementing the well-established capabilities of LD and CD.

Recent studies indicate that trochoidal polarizations can characterize rotational symmetries at interfaces, relevant for studying the coupling between molecules in self-assembled rings, such as those in light-harvesting complexes.[32-33] Mitsch *et al.* have observed that trochoidal polarizations can promote electronic transitions in magnetic fields[34] and Mathevet *et al.* have observed magnetic-field induced CD using trochoidal light.[35] In our recent study, we observed TD in the absence of a magnetic field by characterizing the differential scattering of single orthogonal plasmonic nanorod dimers irradiated by trochoidal waves rotating in opposite directions.[24] We found that the excitation of coupled plasmon modes in the nanorod dimers depends on the direction of trochoidal rotation. However, an understanding of the symmetry properties driving sensitivity to trochoidal field motion is still missing and is required to develop novel spectroscopies utilizing the polarization states of confined light. Moreover, an understanding of near-field polarization-dependent optical properties is needed for uncovering efficient nanoantenna design principles.[36-37]

Here, we explore trochoidal differential scattering as a function of nanoparticle symmetry. We lithographically fabricate single gold nanorods, dimers, and higher-order oligomers and investigate their scattering under trochoidal polarizations of opposite rotational directions. We find that only nanorod assemblies with reduced symmetry, containing one mirror

plane or fewer, feature selective excitation of hybridized plasmons based on the trochoidal polarization. We note that the sign of the TD is modulated by the 0° or 180° orientation of the studied geometries with the direction of light propagation, and thus refer to this property as extrinsic, as the overall experiment geometry induces sensitivity to the direction of trochoidal rotation. We observe that nanodimers in the C_1 point group, which have only identity symmetry, exhibit TD but also have contributions from LD that limit the observed trochoidal differential scattering for two of the four possible isomers. We further discover that analogous to helical plasmonic assemblies with strong CD,[38-39] nanorod trimers and pentamers arranged in a fan-shape tracing the arch of the trochoid exhibit TD and have no isomers with reduced polarization sensitivity.

Methods:

Single-particle spectroscopy: Single-particle scattering spectra were acquired on an inverted dark-field microscope (Zeiss, Axio Observer, m1) with excitation from a quartz-tungsten-halogen lamp (Newport 66884). The light from the lamp was delivered by fiber optic cable to a home-built rail system consisting of a collimating lens (Thorlabs AC254-030-A), an IR filter (Thorlabs FGS550) to protect the film polarization optics, and a linear polarizer (Thorlabs LPVIS100). Light polarized at ±45˚ relative to the E_p axis of the polarizer (Figure 1A) was then focused by a 3 cm lens (Thorlabs AC254-030-A) onto an equilateral prism. For total internal reflection (TIR) conditions, the incident angle onto the prism was ~55° relative to the sample normal and was ~27° for oblique incidence experiments. The scattered light from the particles was collected with a 50x objective with a numerical aperture (NA) = 0.8 (Zeiss) for TIR experiments, and a 40x objective with an extra-long working distance (Zeiss, NA = 0.6) for

oblique incidence experiments. The collected light was passed through the body of the microscope and imaged onto a spectrograph (Acton SpectraPro 2150i) and charge-coupled device camera (Princeton Instruments PIXIS 400BR). Single-particle scattering spectra were collected in a hyperspectral fashion described previously.[40] Briefly, the spectrograph and camera were mounted on a stage that was advanced by a linear actuator (Newport LTA-HL). A slit aperture placed before the camera and spectrograph allowed the collection of multiple spectrally resolved slices as the detection assembly moves across the field of view. The collected spectra are analyzed using scripts written in MATLAB R2017a that perform background subtraction and white-light correction. To account for spectra with partial bonding and antibonding mode excitation, all spectra are fit using non-linear least squares fitting to a sum of two Lorentzian curves, from which the peak wavelength is extracted.

Electron beam lithography: Indium tin oxide (ITO) coated coverglass (Delta Technology LTD CG-50IN-S107) was washed in sequential ten-minute sonication steps with a 2% V/V solution of Hellmanex® detergent, MilliQ water, and ethanol. Then, the slides were cleaned with an O_2 -plasma for two minutes to remove any remaining carbon contamination on the ITO. Next, a layer of positive-tone electron resist, poly (methyl methacrylate) (PMMA A4, Kayaku Advanced Materials), was spin-coated onto the ITO for 60 seconds at 4000 revolutions per minute. The PMMA was baked for 90 seconds at 180°C. The samples were then taken to an FEI Quanta 650 scanning electron microscope (SEM), equipped with a Nanometer Pattern Generation System and beam block. Patterns were written at 30kV with a current of 40pA, a working distance of 7mm and a dose of 500μC/cm^2. The individual rods in each pattern were designed to be 40 nm wide and 80 nm long. The designed gap sizes between each rod, defined as the minimum distance between each rod, was 20 nm for all dimer and oligomer samples. The orthogonal

dimers had a designed interparticle angle of 90˚ and the trimers and pentamers had an interparticle angle between each neighboring rod of 45˚. Each patterned array contained all possible isomers of the species in equal numbers. For example, each array of the orthogonal dimers contained all four isomers: ⅃-, ⅂-, ⌜- and ⌞-dimers so that the single-particle scattering is characterized across all isomers in the same hyperspectral scan. The single rods, parallel dimers, and end-to-end dimers were oriented at angles ranging from 0˚-180˚ in 30˚ steps to sample any orientation-dependent contribution to trochoidal differential scattering.

Once patterned, the resist was developed in a 1:3 methyl isobutyl ketone: isopropyl alcohol solution for 70 seconds and rinsed in isopropyl alcohol for 60 seconds before gently drying with N_2. Then the samples were taken to an electron beam evaporator where 2 nm of Ti (Kamis) was evaporated on the ITO to support adhesion, followed by 40 nm of Au (Kamis). The samples were then placed overnight in acetone and excess Ti and Au were removed through gentle, brief sonication, and drying with N_2.

Finite difference time domain (FDTD) simulations: Numerical simulations of all structures were performed using the Lumerical FDTD software package. The individual nanorod dimensions were tuned to be within 5 nm of the designed dimensions to achieve a good spectral match. The dimers were simulated with a nanorod length of 85 nm and a width of 35 nm, with a 15 nm interparticle gap. For the trimers and pentamers, the lengths and widths of the nanorods were 80 nm and 40 nm, respectively, with an interparticle gap of 20 nm. The nanorods were modeled considering a 2 nm Ti adhesion layer and 40 nm Au thickness. The dielectric function of Au was acquired from Johnson and Christy,[41] and that of Ti was extracted from Palik.[42] The dielectric functions were fit to a Drude-Lorentz model to be used in the FDTD calculations. The interparticle angles of the nanorods matched those of the experiment. The structures were

modeled on a substrate consisting of glass (refractive index n =1.52) and 160 nm of ITO with a wavelength-dependent refractive index of $n \approx 1.7$.[43] The excitation light was polarized at $E_s = \pm E_p$ and was incident through the substrate medium at a 55˚ angle in the TIR case and at a 39˚ angle in the oblique case, as in experiments. Perfectly matched layers surrounded the structures, to avoid reflections from the boundaries. The collection angle of the objective was accounted for by using a square monitor positioned past the decay length of the evanescent field while adjusting its size to collect the scattering from a solid cone. To simulate TIR experiments, the collected cone ranged from 0˚ to 55˚, corresponding to a NA of ~0.8, consistent with experiments. To simulate oblique incidence excitation conditions, the collection cone covered 0˚ to 37˚, corresponding to a NA of 0.6. The charge plots were calculated using a three-dimensional monitor around the structures, calculating the charge density at each point. To generate the two-dimensional charge plots shown, the charges were summed over the height of the structures.

Results and Discussion:

We use total internal reflection (TIR) of linearly polarized light at a glass-air interface to produce a surface-confined evanescent wave with clockwise (CW) and anticlockwise (ACW) trochoidal polarizations (Figure 1A). An evanescent wave formed by TIR has a complex wavevector with an imaginary component perpendicular to the interface, causing the surface confinement, and a real component, $\boldsymbol{k}$, that is parallel to the interface.[44] To maintain orthogonality between the wavevector and field components, evanescent waves contain oscillations that are both transverse and longitudinal to $\boldsymbol{k}$.[45] Trochoidal field motion arises when there is a phase offset between the transverse and longitudinal oscillations.[28] The phase offset is modulated by the incident polarization in terms of E_s and E_p,[28] which are the linear polarization

components perpendicular and parallel to the plane of incidence, respectively (Figure 1A). TIR of light linearly polarized at $-45°$, corresponding to $E_s = -E_p$, yields a 113° phase delay between the in-plane transverse and longitudinal oscillations, giving rise to CW trochoidal polarization (Supporting Information, Figure S1).[24] To achieve ACW trochoidal polarization, the incident polarization is switched to $E_s = E_p$ (45°), producing a -67° phase delay between the in-plane oscillations (Supporting Information, Figure S1). The isolated in-plane components of both CW and ACW trochoidal polarizations are presented in Figure 1B.

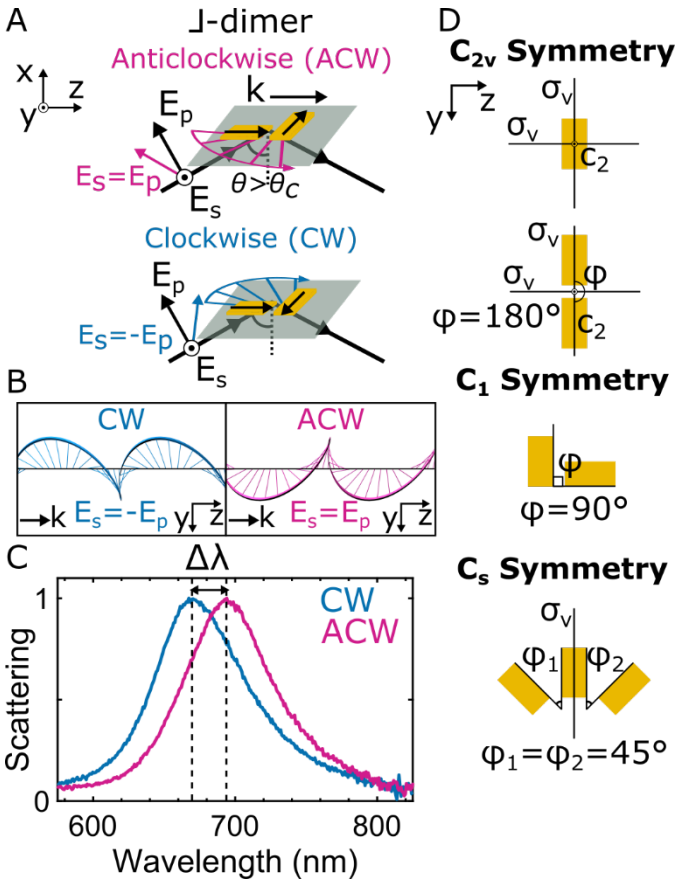

Figure 1: Differential plasmon mode excitation is an indicator of TD. (A) TIR of polarized light gives a polarized evanescent wave. θ: incident angle exceeding the critical angle, θ_c. E_s and E_p are the incident light polarization components. ACW and CW trochoidal polarizations can preferentially excite higher- and lower-energy antibonding and bonding plasmon modes in

orthogonal plasmonic nanorod dimers arranged in a ⌟-shape. (B) ACW and CW trochoidal polarizations resulting from TIR of $E_s = E_p$ (45˚) and $E_s = -E_p$ (−45˚) incident polarizations. (C) Normalized representative single-particle scattering spectrum of a ⌟-dimer under CW and ACW trochoidal excitation. The wavelength difference between the two plasmon modes is indicative of TD. (D) Summary of geometries characterized. φ: interparticle angle, σ_v: plane of mirror symmetry, and C_2: axis of 180˚ rotational symmetry. Single nanorods and dimers with $\varphi = 180^{\circ}$ have C_{2v} symmetry. Orthogonal nanorod dimers have low symmetry and belong to the C_1 point group. Trimers with symmetric substituents off the central nanorod have a single plane of mirror symmetry and belong to the C_s point group. All nanoparticle assemblies possess identity symmetry.

TD gives rise to the selective excitation of bonding and antibonding plasmon modes in coupled metallic nanoparticles. Nanoparticles in close proximity form hybridized, or coupled, plasmon modes, analogous to coupled atomic orbitals in molecular orbital theory.[46] Depending on the symmetry of the nanostructure, CW or ACW trochoidal polarizations preferentially couple to lower-energy bonding or higher-energy antibonding plasmons. If we consider CW trochoidal polarization incident from the left on a dimer of horizontally-offset orthogonal nanorods arranged with one nanorod parallel to $\boldsymbol{k}$ and the other perpendicular to $\boldsymbol{k}$, the polarization aligns with the long axes of both nanorods (Figure 1A). We call this dimer a ⌟-dimer based on the parallel, then perpendicular, arrangement of the nanorods with respect to $\boldsymbol{k}$, which throughout this manuscript, is incident from the left. The longitudinal plasmons of the nanorods in the ⌟-dimer are accordingly excited tail-to-tail under CW polarization, represented by the black arrows in Figure 1A. This high-energy charge configuration constitutes an antibonding plasmon mode,[46] and yields a blue-shifted resonance at 670 nm in the single-particle

scattering spectrum (Figure 1C). By similar symmetry considerations, the polarization of ACW excitation aligns with the first nanorod, but anti-aligns with the vertical nanorod, giving a lower-energy bonding mode and a red-shifted single-particle scattering resonance at 695 nm. The selective excitation of bonding and antibonding modes yields both positive and negative bands in the calculated ACW-CW difference spectrum (Figure S2), similar to the CD spectra of coupled-oscillators following the Born-Kuhn model.[7] As a simple indicator of the differential plasmon mode excitation, we utilize the resonance shift ($\Delta\lambda$) from scattering spectra collected under opposite trochoidal polarizations and display all spectra with normalized intensities to readily observe changes in peak wavelength (Figure 1C). In this work, we characterize the trochoidal-polarization induced resonance shifts of nanoparticle assemblies belonging to the C_{2v}, C_s, and C_1 point groups, with two, one, and zero planes of mirror symmetry, respectively (Figure 1D). Note that although the structures are depicted as planar, due to the presence of a substrate, the particles are not considered to have mirror symmetry with respect to the (y, z) sample plane.[47-48]

The resonance wavelength of single nanorods does not depend on the trochoidal polarization of the excitation. A single nanorod adhered to a substrate belongs to the C_{2v} point group, with two planes of mirror symmetry along the long and short axes, and a single axis of C_2 rotational symmetry. The longitudinal plasmon of a nanorod is responsible for the dominant peak observed in single-particle scattering spectra[49] (Figure 2A) and has an energy primarily dependent on the nanorod's aspect ratio, surroundings, and composition.[50-51] Accordingly, the resonance position of a single nanorod we lithographically fabricate to be 40 nm in width and 80 nm in length does not depend on either the trochoidal (Figure 2A) or the linear polarization (Figure S3) of the excitation. Small resonance shifts may be due to experimental error in focus drift, contributions from LD, or sample imperfections. We therefore use the mean and standard

deviation of a Gaussian fit to a distribution of resonance shifts extracted from 55 nanorods under CW and ACW polarizations to calculate that 95% of the values fall within ±4 nm (Figure 2B). We therefore assign ±4 nm as the experimental trochoidal differential scattering error, which we mark with pink dashed vertical lines in the histogram (Figure 2).

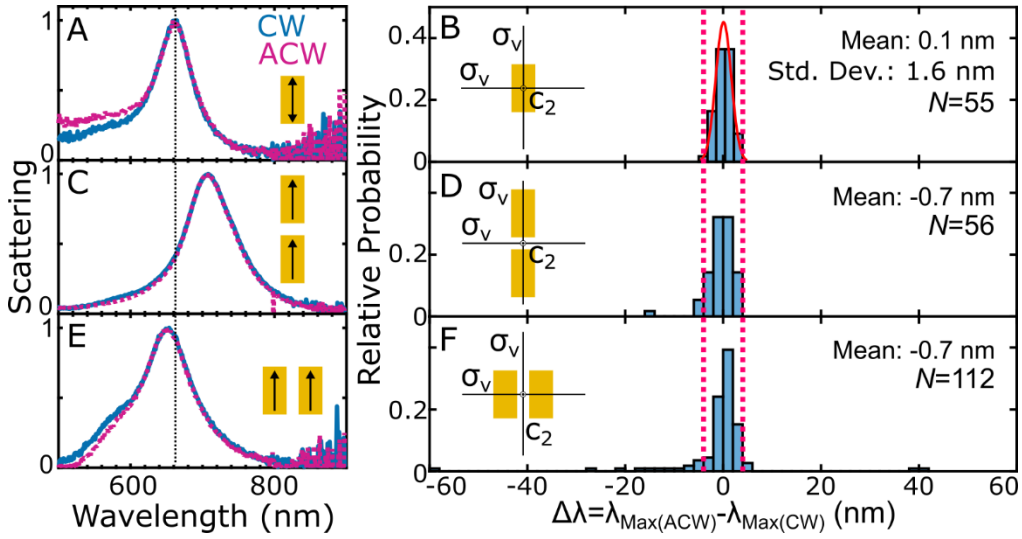

Figure 2: Particles with C_{2v} symmetry do not exhibit significant resonance shifts under CW and ACW trochoidal polarizations. Normalized scattering spectra of (A) single nanorods, (C) end-to-end dimers, and (E) side-by-side dimers under CW and ACW trochoidal excitations. Insets show the orientation of the longitudinal dipoles in the dimers that give a significant net dipole, represented as black arrows. The dashed black vertical line marks the peak scattering wavelength of the single nanorod in panel A. Histograms of resonance shifts for (B) single nanorods, (D) end-to-end dimers, and (F) side-by-side dimers extracted from Lorentzian fits of each single-particle scattering spectrum under CW and ACW trochoidal polarizations. Insets depict the symmetry elements for each nanostructure. The red line in (B) is a Gaussian fit to the distribution of resonance shifts of single nanorods, which has also been presented elsewhere.[24] The mean and standard deviation indicate that 95% of the distribution lies within ±4 nm, which we assign as the

experimental error of trochoidal differential scattering measurements and mark with pink dashed lines on subsequent histograms. *N*: number of independent samples.

Nanorod assemblies with C_{2v} symmetry also do not exhibit changes in their peak scattering wavelength when switching between CW and ACW trochoidal polarizations. The energies of hybridized plasmons depend on the individual nanoparticle's resonance,[52] the interparticle spacing and orientation,[53-54] and the polarization of the excitation.[55] Consistent with previous reports,[53, 56] we find that the resonance wavelength of two 40 nm × 80 nm nanorods arranged end-to-end with a 20 nm interparticle gap red-shifts relative to that of a single nanorod (Figure 2C). The 20 nm gap allows for the individual plasmons to electrostatically couple[57] and only a bonding charge configuration, with the individual dipoles aligned tail-to-tip has a net dipole moment that can strongly scatter to the far-field (Figure 2C-inset).[54] The antibonding mode has a diminished net dipole that does not meaningfully contribute to the scattering spectrum.[54] For side-by-side nanorod dimers offset by 20 nm, only the antibonding plasmon, with constituent dipoles aligned tail-to-tail, has a significant net dipole moment.[54] We find that the peak scattering wavelength of a side-by-side dimer is blue-shifted from that of a single rod (Figure 2E), in agreement with previous observations.[56] The excitation of the bonding plasmon in end-to-end dimers and that of the antibonding plasmon in side-by-side dimers is not accompanied by any rotation of the constituent dipole orientations. As a result, symmetric dimers do not exhibit significant resonance shifts when switching between CW and ACW polarizations in either the single-particle scattering spectra (Figure 2C, E), or in distributions of 56 end-to-end and 112 side-by-side dimers (Figure 2D, F).

With the introduction of an interparticle angle deviating from 0˚ or 180˚, a planar rotation of dipole orientations occurs upon excitation of the hybridized plasmon modes, inducing sensitivity to trochoidal polarizations. The ⅃-dimers, discussed above, have an interparticle angle of 90˚ and belong to the C_1 point group as they only have identity symmetry. Unlike their symmetric dimer counterparts, both the bonding and antibonding modes of ⅃-dimers have net dipole moments and are readily observable in single-particle scattering spectra.[54] CW trochoidal polarization has the proper symmetry to excite both longitudinal dipoles of the ⅃-dimer tail-to-tail, inducing a CW rotation of the constituent dipole orientations in the plane. The scattering from this antibonding plasmon yields a blue-shifted resonance at 670 nm (Figure 3A dashed line). ACW trochoidal polarization excites a red-shifted bonding mode, which scatters at 700 nm for this particular ⅃-dimer (Figure 3A dotted line).

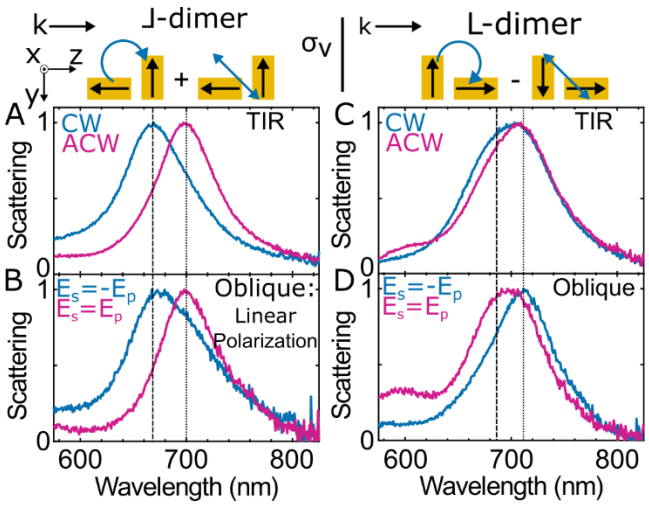

Figure 3: ⅃-dimers and L-dimers have similar TD contributions to their differential plasmon mode excitation but opposing LD contributions. Trochoidal polarization sensitivity for L-dimers is reduced by the linear components of the trochoidal excitation. (A) Normalized single-particle scattering spectra of a ⅃-dimer under CW and ACW trochoidal excitation and (B) under oblique $E_s = \pm E_p$ incident light. (C) Normalized single-particle scattering spectra of an L-dimer under

CW and ACW trochoidal excitation and (D) under oblique $E_s = \pm E_p$ incident light. Dashed and dotted vertical lines are placed at the resonance wavelength of the antibonding and bonding mode, respectively. Cartoons above the spectra depict plasmon mode excitations driven by the rotational and linear components of CW trochoidal polarization, where black arrows represent the longitudinal dipoles of the nanorods excited tail-to-tail or tip-to-tail depending on the dimer's geometry.

Evanescent waves produced by TIR of linearly polarized light naturally possess linear components, which can contribute to the differential excitation of bonding and antibonding plasmons in the asymmetric dimers. The linear components cause the arch of the trochoid to lean at approximately ±70° angles away from $\boldsymbol{k}$ in the (y, z) sample plane for TIR of $E_s = \pm E_p$ light (Figure 1B and Figure S1). $E_s = \pm E_p$ light incident at an oblique angle produces only linear polarizations, and the components projected into the (y, z) sample plane are polarized at ±70° (Supporting Information, Figure S4). To characterize the role of the linear components in the trochoidal differential scattering, we thus measure the scattering of the dimers under oblique incidence linearly-polarized excitation. The net dipole of the ⊥-dimer's antibonding mode coincides with the -45° axis in the (y, z) sample plane (Figure 3A cartoon). Oblique incident $E_s = -E_p$ (-45°) polarized light couples with the blue-shifted antibonding mode, while oblique incident $E_s = E_p$ light excites the bonding mode (Figure 3B). Therefore, the resonance shifts measured under opposite trochoidal and linear polarizations of the ⊥-dimer are of the same sign and of a similar magnitude. We expect that the linear and rotational components of the excitation work synergistically to selectively promote the bonding and antibonding plasmons observed in the trochoidal differential scattering of the ⊥-dimer (Figure 3A cartoon).

L-shaped dimers are the mirror image of the ⅃-dimer over the (x, y) plane and have TD and LD contributions of opposite sign, leading to mode-mixing when excited by CW and ACW trochoidal polarizations. With a fixed ***k*,** CW trochoidal excitation still aligns with both nanorods of the L-dimer, promoting antibonding mode excitation (Figure 3C cartoon). Indeed, CW excitation given by TIR of $E_s = -E_p$ light yields a blue-shifted shoulder in the trochoidal differential scattering of the L-dimer (Figure 3C dashed line). The net dipole of the bonding mode lies along the -45°axis in the (y, z) plane (Figure 3C cartoon). Therefore, oblique incident $E_s = -E_p$ (-45°) light excites the bonding mode (Figure 3D dotted line), while $E_s = E_p$ (45°) light dominantly promotes the antibonding mode (Figure 3D dashed line). While developing a method to formally correct for the linear components of the trochoidal excitation is the subject of future work, we observe opposite TD- and LD-driven mode excitations in the L-dimers. The differing polarization sensitivity of the L-dimers under TIR and oblique excitation conditions demonstrates that our trochoidal differential scattering results are not only due to LD, enabling a distinction between the two dichroisms. This result is well reproduced in the simulated scattering spectra (Figure S5). However, the competing action of the rotational and linear components in the trochoidal excitation leads to the simultaneous excitation of both bonding and antibonding modes under CW and ACW polarizations (Figure 3C, cartoon). As a result, the L-dimer has reduced trochoidal polarization sensitivity compared to the ⅃-dimer.

Dimers with C_1 symmetry have four possible isomers, each with distinct trochoidal and linear differential scattering. The four isomers are related by mirror symmetry operations. In principal, any mirror operation reverses the sign of the LD but only mirroring over the (x, z) plane containing ***k*** gives TD of the opposite sign. As shown in Figure 3A and B, ⅃-dimers have similar mode excitations driven by trochoidal and linear polarizations, and give resonance shifts of

similar magnitude, confirmed over a distribution of 37 ⅃-dimers characterized under both TIR and oblique incidence excitation geometries (Figure 4A). The mirror image of the ⅃-dimer over the (x, z) plane containing ***k*** forms a ⅂-dimer and reverses the sign of both the TD- and LD-dependent resonance shifts relative to those of the ⅃-dimers (Figure 4B). Similar in behavior to the ⅃-dimer, ⅂-dimers also have TD and LD contributions of the same sign, giving indistinguishable resonance shift distributions for both dichroisms (Figure 4B).

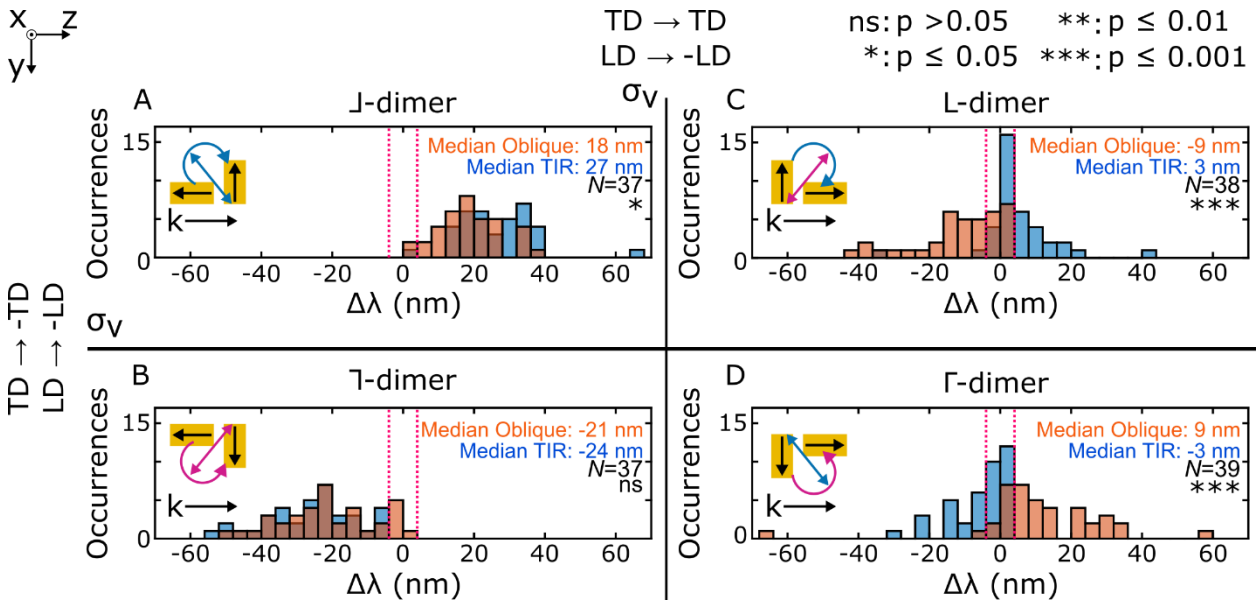

Figure 4: Histograms of resonance shifts of the four possible isomers of orthogonal nanorod dimers under both TIR and oblique excitation geometries with $E_s = E_p$ (45˚) and $E_s = -E_p$ (−45˚) incident polarizations. The TIR excitation geometry characterizes TD, shown in blue bins, while the oblique incidence geometry characterizes LD shown in orange bins. The resonance shifts are extracted from Lorentzian fits of the dimers and are calculated as $\Delta\lambda = \lambda_{\max(E_s=E_p)} - \lambda_{\max(E_s=-E_p)}$ (nm). Although an objective lens with a lower NA than that used for TIR excitation is required to collect the scattering under oblique incidence excitation, the resonance shift distributions of the dimers do not significantly depend on the NA of the

collection optics (Figure S6, Table S2). (A, B) The ⅃- and ⅂- dimer isomers have similar resonance shift distributions under trochoidal and linear polarizations that are not significantly distinguishable across both isomers. (C, D) The L- and Γ- dimer isomers predominantly exhibit TD- and LD-driven resonance shifts of opposite sign. Inset cartoons depict the dimer geometry and the trochoidal and linear polarizations expected to excite an antibonding mode, represented by black arrows showing the tail-to-tail arrangement of longitudinal dipoles in the nanorods. Each isomer is related by mirror-image operations (σ_v). A mirror across the (x, y) plane maintains the sign of the TD contribution to the differential scattering, while reversing that of the LD, enabling distinction of the two dichroisms. The Kolmogorov-Smirnov test is employed to assess statistical difference between resonance shift distributions measured under TIR and oblique incidence excitation (Table S1). One to three asterisks indicate p-value ranges of 95%, 99%, and 99.9% confidence for statistical difference, respectively, while ns signifies that the distributions are not statistically different at the 95% confidence level. *N* is the number of independent samples.

L- and Γ-dimers predominantly have TD- and LD-driven resonance shifts of opposite sign, enabling a clear distinction of the two dichroisms in these isomers. As shown in Figure 3C and D above, trochoidal and linear polarizations promote opposite differential-mode excitation in the L-dimer. Over a distribution of 38 L-dimers, the sign of the median resonance shift measured under trochoidal polarizations is opposite that due to LD (Figure 4C). The Γ-dimer is the mirror image of the L-dimer over the (x, z) plane containing $\boldsymbol{k}$, switching the sign of both the TD- and LD-dependent resonance shifts (Figure 4D). For these two isomers, trochoidal and linear polarizations promote opposite hybridized plasmon modes, enabling a significant distinction

between TD and LD (Figure 4C, D). To quantify this difference, the non-parametric Kolmogorov-Smirnov test confirms that the resonance shift distributions under TIR and oblique excitations are statistically distinct for both ⌞- and ⌜-dimers with 99.9% confidence (p-value < 0.001) (Figure 4C, D; Table S1). However, the magnitude of the resonance shifts observed in the ⌞- and ⌜-dimers is reduced relative to those of the ⌟- and ⌝-dimers due to competing contributions of the rotational and linear components in the trochoidal excitation. Finally, we note that each of the dimer isomers can also be related by a 180° rotation. For example, rotating a ⌟-dimer 180° yields a ⌜-dimer (Figure 4A, D). With ***k*** maintained, a 180° rotation is expected to give opposite TD-driven mode excitations but maintain the linear contributions. Accordingly, the ⌟-dimers and ⌜-dimers exhibit median resonance shifts of opposite sign under trochoidal polarizations, while the sign of the LD-dependent resonance shifts are maintained for both isomers (Figure 4A, D).

Nanoparticle trimer assemblies with C_s symmetry have only two isomers and both have hybridized plasmon modes that are selectively excited by opposite trochoidal polarizations. Nanorod trimers with components arranged in a fan-shape have a plane of mirror symmetry in the (x, y) plane perpendicular to ***k*** and possess identity symmetry. They therefore belong to the C_s point group and have up-facing and down-facing isomers related by a mirror operation over the (x, z) plane containing ***k*** (Figure 5A, B). Single-particle scattering spectra of the up-facing trimer reveal that CW trochoidal field motion effectively couples to an antibonding mode at 677 nm (Figure 5A dashed line), while ACW polarization excites a red-shifted mode at 700 nm (Figure 5A dotted line). The down-facing trimer has the opposite trochoidal-dependent mode excitations, with ACW polarization giving the antibonding mode (Figure 5B dashed line). Due to their mirror symmetry with respect to the (x, y) plane, the up- and down-facing trimers are

interconverted by either a mirror operation over the (x, z) plane or by a 180° rotation. The sign of the resonance shift under opposite trochoidal polarizations is determined by the 0° or 180° orientation with respect to ***k*** (Figure 5A, B). The dependence on ***k*** is analogous to extrinsic chirality, in which nanostructures with mirror symmetry, but a chiral experiment geometry, give rise to CD.[55, 58]

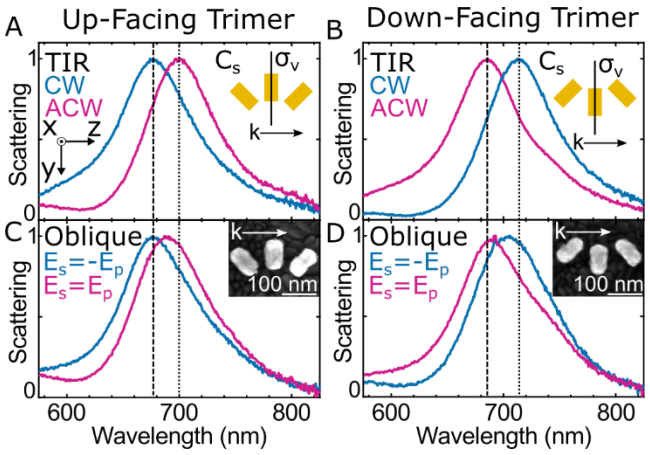

Figure 5: CW and ACW trochoidal polarizations selectively promote bonding and antibonding modes in trimers with C_s symmetry while linear polarizations yield reduced resonance shifts. (A) Normalized single trimer scattering spectra under CW and ACW trochoidal polarizations and (C) under oblique $E_s = \pm E_p$ incident light. Insets: cartoon depiction of the trimers with marked planes of mirror symmetry as well as SEM images of the trimers. Dashed and dotted vertical lines mark the resonance wavelengths of the antibonding and bonding-type plasmons, respectively. (B, D) same as A and C but for a mirror-image trimer. The resonance shifts resulting from LD are reduced relative to those driven by TD for both up- and down-facing trimer isomers.

The vertical mirror symmetry of the trimers reduces their sensitivity to linear polarizations. In the up-facing trimer, $E_s = -E_P$ light incident at an oblique angle excites a blue-shifted resonance at 677 nm (Figure 5C dashed line), consistent with the resonance position we observe with CW trochoidal excitation (Figure 5A dashed line). However, oblique $E_s = E_p$ light excites a resonance red-shifted by only 13 nm (Figure 5C), compared to the 23 nm shift we observe under trochoidal polarizations (Figure 5A). The down-facing trimer has a resonance shift of 14 nm under the two linear polarizations, with $E_s = E_p$ light now exciting the blue-shifted resonance (Figure 5D). As with the ⅃- and ⅂-dimers described above, we expect the linear components of the trochoidal excitation work together with the rotational components to promote strong differential plasmon mode excitation in the trimers. However, the resonance shifts due to LD are reduced relative to those observed under trochoidal polarizations, enabling a distinction between the two dichroisms. Simulations of the trimers confirm that they have TD- and LD-dependent resonance shifts of the same sign, with comparatively weak linear polarization sensitivity (Figure S7).

The differential excitation of bonding and antibonding plasmons in trimers under CW and ACW polarizations results from the fan-shaped arrangement of nanorods tracing out the arch of the trochoid. Due to the finite horizontal offset between adjacent nanorods, all three nanorods simultaneously experience different phases of the excitation (Figure 6A, B). Figure 6A, B shows CW and ACW trochoidal polarizations overlaid with an accurately scaled trimer. When the up-facing trimer is excited by CW trochoidal polarization, the electric field aligns with all three nanorods in the curved arrangement (Figure 6A). Accordingly, all three dipoles of the nanorods are excited in-phase (Figure 6A). This high-energy charge accumulation yields a blue-shifted antibonding plasmon in simulated spectra (Figure 6C). When the excitation is switched to ACW,

the field predominantly aligns with the first nanorod, but anti-aligns with the remaining two nanorods in the trimer (Figure 6B), exciting the first two nanorods' dipoles out-of-phase and giving a red-shifted bonding configuration (Figure 6C). While in a pure bonding mode, the central nanorod's dipole is out-of-phase with both neighboring dipoles, this mode has a diminished net dipole and cannot be efficiently excited. Rather, we expect a coupled plasmon with bonding character, with only the first two dipoles out-of-phase, reducing the energy of the mode relative to the all in-phase antibonding mode, while still allowing a significant net dipole. Charge distributions calculated at the peak scattering intensity confirm these expectations, with antibonding and bonding plasmons dominantly excited with CW and ACW trochoidal polarizations, respectively (Figure 6D, E). Simulated spectra of V-shaped nanorod dimers yield similar trochoidal differential scattering (Figure S8), indicating the generality of our conclusions to many nanoparticle arrangements with C_s symmetry.

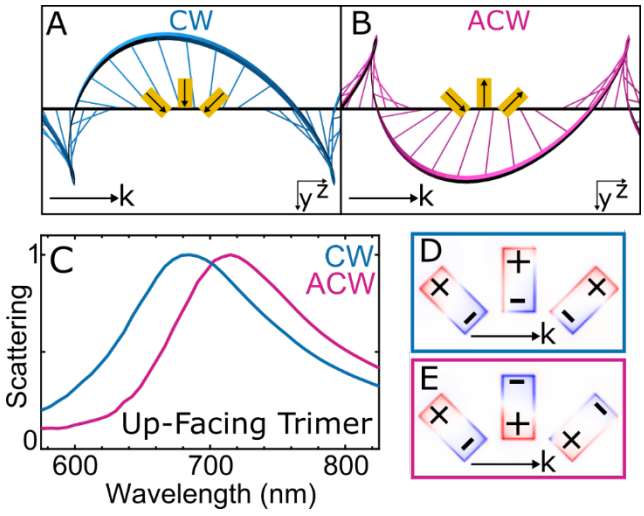

Figure 6: Trimers (C_s symmetry) exhibit TD due to their fan-shape approximately following the curve of the trochoid. (A, B) CW and ACW trochoidal polarizations are overlaid with an

accurately scaled up-facing trimer. When switching from CW to ACW polarizations, the individual dipoles shift from all in-phase, giving an antibonding mode, to out-of-phase, forming a bonding configuration. (C) Normalized simulated scattering spectra of the trimers under CW and ACW trochoidal polarizations. Charge distributions of the trimer calculated at the peak scattering intensity under (D) CW and (E) ACW trochoidal excitation confirm differential promotion of antibonding and bonding plasmons under opposite polarizations.

Pentamer nanoparticle assemblies are sensitive to the direction of trochoidal rotation and have a fan-shape that extends to include nanorods directly aligned with $\boldsymbol{k}$, further matching the arch of the trochoid. Similar to the trimers, simulations confirm that CW polarization can excite all five dipoles of an up-facing pentamer in-phase (Figure S9), yielding an antibonding mode at 675 nm (Figure 7A dashed line). Under ACW trochoidal excitation, the resonance red-shifts 20 nm to 695 nm (Figure 7A dotted line). Mirror-image pentamers across the (x, z) plane give the opposite resonance shift with ACW trochoidal polarization exciting the antibonding mode (Figure 7B). The magnitude of the resonance shifts in the pentamers is similar to that of the trimers, indicating that nanoparticle assemblies with C_s symmetry can exhibit strong TD, even without completing a full trace of the arch. The similar magnitude of the resonance shifts between the two geometries is likely a result of maintaining a 20 nm separation between the individual rods in each nanoparticle assembly, limiting the maximum difference in peak wavelength between the two modes. Oblique incident $E_s = \pm E_p$ light promotes resonances between the bonding and antibonding modes in energy with reduced wavelength differences relative to those measured under opposite trochoidal polarizations (Figure 7C, D). $E_s = -E_p$ light excites a resonance at 680 nm in the up-facing pentamer, minimally blue-shifted from that

excited by oblique incident $E_s = E_p$ light at 690 nm (Figure 7C). The down-facing pentamer has the opposite resonance shift due to LD, and $E_s = E_p$ light excites the blue-shifted resonance (Figure 7D). Simulations confirm that both isomers of the pentamers exhibit differential excitation of bonding and antibonding plasmons under trochoidal polarizations, with weak linear polarization sensitivity (Figure S9).

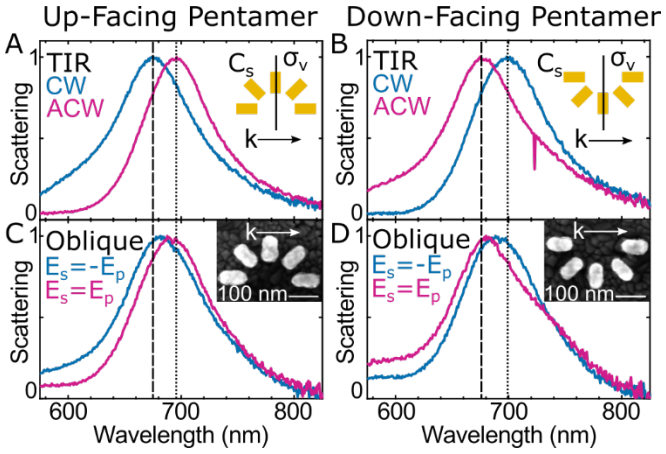

Figure 7. Pentamers with C_s symmetry have trochoidal differential scattering with reduced resonance shifts under linear polarizations. Normalized single pentamer scattering spectra under (A) CW and ACW trochoidal polarizations and (C) under oblique $E_s = \pm E_p$ incident light. Insets: Schematic of the pentamers with symmetry elements noted and SEM image of a pentamer. Vertical dashed and dotted lines identify the resonance wavelengths of the modes with antibonding and bonding character, respectively. (B, D) same as A and C for a mirror-image pentamer across the (x, z) plane containing $\boldsymbol{k}$. Similar to the trimers, the pentamers have differential interactions with trochoidal polarizations as a result of their fan-shape, which approximately traces the curved arch of the trochoid.

On average, for fan-shaped oligomers with C_s symmetry, trochoidal polarizations selectively promote bonding and antibonding plasmons, while the differential mode excitation due to LD is suppressed. Figure 8 shows a box plot of resonance shifts extracted from Lorentzian fits of single-particle scattering spectra of the trimers and pentamers acquired under TIR and oblique excitation conditions. Across all geometries characterized, the resonance shifts induced by TD are significantly greater than those induced by LD. As a result, although the resonance shifts driven by LD and TD are of the same sign for the fan-shaped assemblies, the effects due to TD are easily distinguishable. Moreover, unlike the asymmetric dimers, there is not an isomer of the trimers or pentamers with reduced sensitivity to CW and ACW trochoidal polarizations.

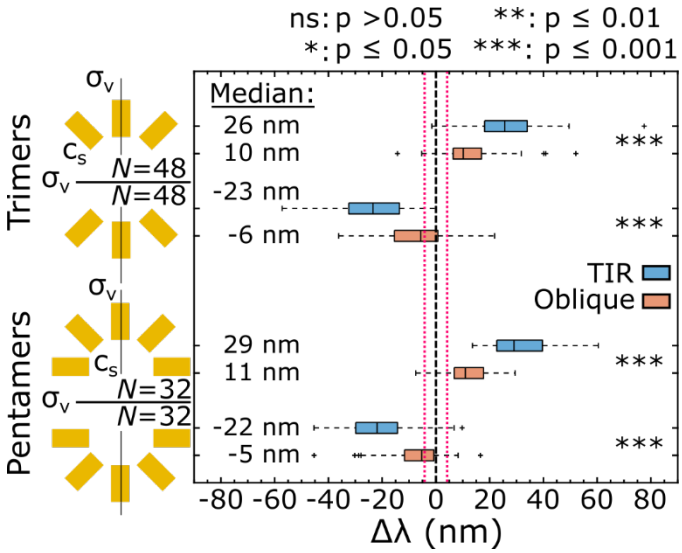

Figure 8: Particles with C_s symmetry exhibit TD- and LD-driven resonance shifts of the same sign, but those measured under trochoidal polarizations are significantly larger in magnitude. Box plot of resonance shifts of 96 trimers and 64 pentamers under both TIR and oblique excitation conditions. The resonance shift is calculated as $\Delta\lambda = \lambda_{\max(E_s=E_p)} -$

$\lambda_{\max(E_s=-E_p)}$ (nm). The top two boxes are the resonance shift distributions from 48 trimers under TIR and oblique incidence excitation, with the next two coming from 48 mirror-image trimers. The bottom 4 boxes are the resonance shift distributions from pentamers, with 32 pentamers for each isomer. Median values for all 8 distributions are printed on the left side of the box plot. The three asterisks on the right side of the box plot denote p-values of ≤ 0.001 calculated by applying the Kolmogorov-Smirnov test to the TIR and oblique incidence data for each geometry, confirming the two excitation conditions yield different distributions with 99.9% confidence. Although an objective lens with a lower NA than that used under TIR excitation is required for dark-field imaging under oblique incident excitation, the resonance shift distributions of the pentamers are not significantly impacted by the collection NA (Figure S10, Table S3).

Conclusions:

In conclusion, only plasmonic nanoantennas with one or fewer planes of mirror symmetry exhibit TD. Nanoparticle assemblies with higher symmetry belonging to the C_{2v} point group are not sensitive to the direction of trochoidal rotation, yet lower-symmetry dimers and fan-shaped assemblies have selective promotion of their plasmon modes based on the trochoidal polarization. Although dimers with C_1 symmetry have a subset of isomers with weak trochoidal differential scattering, all isomers with C_s symmetry have resonances sensitive to the direction of trochoidal rotation. Similar to helical plasmonic structures with large CD,[38-39] fan-shaped structures match the geometry of the trochoidal wave, resulting in significant trochoidal polarization sensitivity. Our results inform the design of efficient polarization-dependent nanoantennas for implementation with near-field confined light.[36] Further, by characterizing the

geometric parameters that drive TD in plasmonic systems, we gain an understanding of the molecular geometries we expect to be sensitive to trochoidal polarization, and thus probable by this new optical tool. Ultimately, molecules exhibiting a planar rotation of charge upon excitation are expected to have TD-active transitions. Examples include achiral molecules with orthogonal electric and magnetic dipole transition moments,[59] and self-assembled rings of electronically-coupled molecules, such as light-harvesting antennas.[32-33] Additionally, trochoidal birefringence measuring the differential refractive index of a material under opposite trochoidal polarizations is expected to accompany TD in molecular and plasmonic systems, forming a complementary technique to optical rotatory dispersion.[60] While the relative strength of TD compared to CD and LD in molecular systems remains to be characterized, the ability to observe signatures of TD on the single-particle level is promising. However, applying TD to molecular systems is currently limited by the requirement of molecular alignment with $\boldsymbol{k}$, which may be possible only in single-molecular assembly experiments.[61] To expand the applicability of TD, future studies will focus on uncovering the symmetry elements required to observe intrinsic trochoidal dichroism, which would elucidate molecular geometries expected to have TD invariant with respect to $\boldsymbol{k}$.

ASSOCIATED CONTENT

Supporting Information. Description and visualization of evanescent and oblique incidence polarization components, ACW-CW difference scattering spectrum of an ⌟-dimer, resonance shift distribution of single nanorods under oblique $E_s = \pm E_p$ incident light, simulated scattering spectra of dimers, trimers, and pentamers under evanescent and oblique incidence excitation,

simulated scattering of V-shaped dimers, and comparison of resonance shift distributions from spectra acquired with different collection NAs.

The following files are available free of charge.

TD_symmetry_SI.pdf

AUTHOR INFORMATION

***corresponding author** slink@rice.edu

Author Contributions

The manuscript was written through the contributions of all authors. All authors have given approval to the final version of the manuscript

ACKNOWLEDGEMENT

This work was funded by grants from the Robert A. Welch Foundation (C-1664) and the National Science Foundation (CHE1903980 and CHE1727122). L. A. M. acknowledges the National Science Foundation Graduate Research Fellowship Program (1842494) for support. We thank the Rice Shared Equipment Authority and Electron Microscopy Center (EMC) for instrument use and availability.

ABBREVIATIONS

LD, linear dichroism; CD, circular dichroism; TD, trochoidal dichroism; TIR, total internal reflection; NA, numerical aperture; CW, clockwise; ACW, anticlockwise

REFERENCES

1. Bustamante, C.; Tinoco, I.; Maestre, M. F., Circular Differential Scattering Can Be an Important Part of the Circular Dichroism of Macromolecules. *Proc. Natl. Acad. Sci. U. S. A.* **1983,** *80*, 3568-3572.

2. Rodger, A.; Dorrington, G.; Ang, D. L., Linear Dichroism as a Probe of Molecular Structure and Interactions. *Analyst* **2016,** *141*, 6490-6498.

3. Hentschel, M.; Schäferling, M.; Metzger, B.; Giessen, H., Plasmonic Diastereomers: Adding up Chiral Centers. *Nano Lett.* **2013,** *13*, 600-606.

4. Hentschel, M.; Schäferling, M.; Weiss, T.; Liu, N.; Giessen, H., Three-Dimensional Chiral Plasmonic Oligomers. *Nano Lett.* **2012,** *12*, 2542-2547.

5. Pettine, J.; Grubisic, A.; Nesbitt, D. J., Polarization-Controlled Directional Multiphoton Photoemission from Hot Spots on Single Au Nanoshells. *J. Phys. Chem. C* **2018,** *122*, 14805-14813.

6. Auguié, B.; Alonso-Gómez, J. L.; Guerrero-Martínez, A. s.; Liz-Marzán, L. M., Fingers Crossed: Optical Activity of a Chiral Dimer of Plasmonic Nanorods. *J. Phys. Chem. Lett.* **2011,** *2*, 846-851.

7. Yin, X.; Schäferling, M.; Metzger, B.; Giessen, H., Interpreting Chiral Nanophotonic Spectra: The Plasmonic Born–Kuhn Model. *Nano Lett.* **2013,** *13*, 6238-6243.

8. Fan, X. F.; Zheng, W. T.; Singh, D. J., Light Scattering and Surface Plasmons on Small Spherical Particles. *Light Sci. Appl.* **2014,** *3*, e179.

9. Gansel, J. K.; Thiel, M.; Rill, M. S.; Decker, M.; Bade, K.; Saile, V.; Freymann, G. v.; Linden, S.; Wegener, M., Gold Helix Photonic Metamaterial as Broadband Circular Polarizer. *Science* **2009,** *325*, 1513-1515.

10. Zhao, Y.; Belkin, M. A.; Alù, A., Twisted Optical Metamaterials for Planarized Ultrathin Broadband Circular Polarizers. *Nat. Commun.* **2012,** *3*, 870.

11. Tanaka, Y. Y.; Shimura, T., Tridirectional Polarization Routing of Light by a Single Triangular Plasmonic Nanoparticle. *Nano Lett.* **2017,** *17*, 3165-3170.

12. Kumar, J.; Eraña, H.; López-Martínez, E.; Claes, N.; Martín, V. F.; Solís, D. M.; Bals, S.; Cortajarena, A. L.; Castilla, J.; Liz-Marzán, L. M., Detection of Amyloid Fibrils in Parkinson's Disease Using Plasmonic Chirality. *Proc. Natl. Acad. Sci. U. S. A.* **2018,** *115*, 3225-3230.

13. Kneer, L. M.; Roller, E. M.; Besteiro, L. V.; Schreiber, R.; Govorov, A. O.; Liedl, T., Circular Dichroism of Chiral Molecules in DNA-Assembled Plasmonic Hotspots. *ACS Nano* **2018,** *12*, 9110-9115.

14. Wang, L. Y.; Smith, K. W.; Dominguez-Medina, S.; Moody, N.; Olson, J. M.; Zhang, H. N.; Chang, W. S.; Kotov, N.; Link, S., Circular Differential Scattering of Single Chiral Self-Assembled Gold Nanorod Dimers. *ACS Photonics* **2015,** *2*, 1602-1610.

15. Smith, K. W.; McCarthy, L. A.; Alabastri, A.; Bursi, L.; Chang, W. S.; Nordlander, P.; Link, S., Exploiting Evanescent Field Polarization for Giant Chiroptical Modulation from Achiral Gold Half-Rings. *ACS Nano* **2018,** *12*, 11657-11663.

16. Biswas, S.; Nepal, D.; Park, K.; Vaia, R. A., Orientation Sensing with Color Using Plasmonic Gold Nanorods and Assemblies. *J. Phys. Chem. Lett.* **2012,** *3*, 2568-2574.

17. Greybush, N. J.; Pacheco-Pena, V.; Engheta, N.; Murray, C. B.; Kagan, C. R., Plasmonic Optical and Chiroptical Response of Self-Assembled Au Nanorod Equilateral Trimers. *ACS Nano* **2019,** *13*, 1617-1624.

18. Smith, K. W.; Zhao, H. Q.; Zhang, H.; Sanchez-Iglesias, A.; Grzelczak, M.; Wang, Y. M.; Chang, W. S.; Nordlander, P.; Liz-Marzan, L. M.; Link, S., Chiral and Achiral

Nanodumbbell Dimers: The Effect of Geometry on Plasmonic Properties. *ACS Nano* **2016,** *10*, 6180-6188.

19. Karst, J.; Cho, N. H.; Kim, H.; Lee, H. E.; Nam, K. T.; Giessen, H.; Hentschel, M., Chiral Scatterometry on Chemically Synthesized Single Plasmonic Nanoparticles. *ACS Nano* **2019,** *13*, 8659-8668.

20. Karst, J.; Strohfeldt, N.; Schäferling, M.; Giessen, H.; Hentschel, M., Single Plasmonic Oligomer Chiral Spectroscopy. *Adv. Opt. Mater.* **2018,** *6*, 1800087.

21. Zhang, Q. F.; Hernandez, T.; Smith, K. W.; Jebeli, S. A. H.; Dai, A. X.; Warning, L.; Baiyasi, R.; McCarthy, L. A.; Guo, H.; Chen, D. H., et al., Unraveling the Origin of Chirality from Plasmonic Nanoparticle-Protein Complexes. *Science* **2019,** *365*, 1475-1478.

22. Kerber, R. M.; Fitzgerald, J. M.; Oh, S. S.; Reiter, D. E.; Hess, O., Orbital Angular Momentum Dichroism in Nanoantennas. *Commun. Phys.* **2018,** *1*, 87.

23. Yang, N.; Cohen, A. E., Local Geometry of Electromagnetic Fields and Its Role in Molecular Multipole Transitions. *J. Phys. Chem. B* **2011,** *115*, 5304-5311.

24. McCarthy, L. A.; Smith, K. W.; Lan, X.; Hosseini Jebeli, S. A.; Bursi, L.; Alabastri, A.; Chang, W.-S.; Nordlander, P.; Link, S., Polarized Evanescent Waves Reveal Trochoidal Dichroism. *Proc. Natl. Acad. Sci. U. S. A.* **2020,** *117*, 16143-16148.

25. Tang, Y.; Cohen, A. E., Enhanced Enantioselectivity in Excitation of Chiral Molecules by Superchiral Light. *Science* **2011,** *332*, 333-336.

26. Hendry, E.; Carpy, T.; Johnston, J.; Popland, M.; Mikhaylovskiy, R. V.; Lapthorn, A. J.; Kelly, S. M.; Barron, L. D.; Gadegaard, N.; Kadodwala, M., Ultrasensitive Detection and Characterization of Biomolecules Using Superchiral Fields. *Nat. Nanotechnol.* **2010,** *5*, 783-787.

27. Solomon, M. L.; Saleh, A. A. E.; Poulikakos, L. V.; Abendroth, J. M.; Tadesse, L. F.; Dionne, J. A., Nanophotonic Platforms for Chiral Sensing and Separation. *Acc. Chem. Res.* **2020,** *53*, 588-598.

28. Bliokh, K. Y.; Bekshaev, A. Y.; Nori, F., Extraordinary Momentum and Spin in Evanescent Waves. *Nat. Commun.* **2014,** *5*, 3300.

29. Bliokh, K. Y.; Nori, F., Transverse Spin of a Surface Polariton. *Phys. Rev. A* **2012,** *85*, 061801.

30. Aiello, A.; Banzer, P.; Neugebauer, M.; Leuchs, G., From Transverse Angular Momentum to Photonic Wheels. *Nat. Photonics* **2015,** *9*, 789-795.

31. Bliokh, K. Y.; Nori, F., Transverse and Longitudinal Angular Momenta of Light. *Phys. Rep.* **2015,** *592*, 1-38.

32. Fujita, T.; Brookes, J. C.; Saikin, S. K.; Aspuru-Guzik, A., Memory-Assisted Exciton Diffusion in the Chlorosome Light-Harvesting Antenna of Green Sulfur Bacteria. *J. Phys. Chem. Lett.* **2012,** *3*, 2357-2361.

33. Ganapathy, S.; Oostergetel, G. T.; Wawrzyniak, P. K.; Reus, M.; Chew, A. G. M.; Buda, F.; Boekema, E. J.; Bryant, D. A.; Holzwarth, A. R.; de Groot, H. J. M., Alternating Syn-Anti Bacteriochlorophylls Form Concentric Helical Nanotubes in Chlorosomes. *Proc. Natl. Acad. Sci. U. S. A.* **2009,** *106*, 8525-8530.

34. Mitsch, R.; Sayrin, C.; Albrecht, B.; Schneeweiss, P.; Rauschenbeutel, A., Exploiting the Local Polarization of Strongly Confined Light for Sub-Micrometer-Resolution Internal State Preparation and Manipulation of Cold Atoms. *Phys. Rev. A* **2014,** *89*, 063829.

35. Mathevet, R.; Rikken, G. L. J. A., Magnetic Circular Dichroism as a Local Probe of the Polarization of a Focused Gaussian Beam. *Opt Mater Express* **2014,** *4*, 2574-2585.

36. Espinosa-Soria, A.; Griol, A.; Martínez, A., Experimental Measurement of Plasmonic Nanostructures Embedded in Silicon Waveguide Gaps. *Opt. Express* **2016,** *24*, 9592-9601.

37. Thomaschewski, M.; Yang, Y. Q.; Wolff, C.; Roberts, A. S.; Bozhevolnyi, S. I., On-Chip Detection of Optical Spin-Orbit Interactions in Plasmonic Nanocircuits. *Nano Lett.* **2019,** *19*, 1166-1171.

38. Kuzyk, A.; Schreiber, R.; Fan, Z.; Pardatscher, G.; Roller, E.-M.; Hogele, A.; Simmel, F. C.; Govorov, A. O.; Liedl, T., DNA-Based Self-Assembly of Chiral Plasmonic Nanostructures with Tailored Optical Response. *Nature* **2012,** *483*, 311-314.

39. Lan, X.; Liu, T. J.; Wang, Z. M.; Govorov, A. O.; Yan, H.; Liu, Y., DNA-Guided Plasmonic Helix with Switchable Chirality. *J. Am. Chem. Soc.* **2018,** *140*, 11763-11770.

40. Byers, C. P.; Hoener, B. S.; Chang, W.-S.; Yorulmaz, M.; Link, S.; Landes, C. F., Single-Particle Spectroscopy Reveals Heterogeneity in Electrochemical Tuning of the Localized Surface Plasmon. *J. Phys. Chem. B* **2014,** *118*, 14047-14055.

41. Johnson, P. B.; Christy, R. W., Optical Constants of Noble Metals. *Phys. Rev. B* **1972,** *6*, 4370-4379.

42. Palik, E. D., *Handbook of Optical Constants of Solids Iii*. Academic Press: San Diego, 1998.

43. Konig, T. A. F.; Ledin, P. A.; Kerszulis, J.; Mahmoud, M. A.; El-Sayed, M. A.; Reynolds, J. R.; Tsukruk, V. V., Electrically Tunable Plasmonic Behavior of Nanocube-Polymer Nanomaterials Induced by a Redox-Active Electrochromic Polymer. *ACS Nano* **2014,** *8*, 6182-6192.

44. Van Mechelen, T.; Jacob, Z., Universal Spin-Momentum Locking of Evanescent Waves. *Optica* **2016,** *3*, 118.

45. Milosevic, M., On the Nature of the Evanescent Wave. *Appl. Spectrosc.* **2013,** *67*, 126-131.

46. Prodan, E., A Hybridization Model for the Plasmon Response of Complex Nanostructures. *Science* **2003,** *302*, 419-422.

47. Nechayev, S.; Barczyk, R.; Mick, U.; Banzer, P., Substrate-Induced Chirality in an Individual Nanostructure. *ACS Photonics* **2019,** *6*, 1876-1881.

48. Arteaga, O.; Sancho-Parramon, J.; Nichols, S.; Maoz, B. M.; Canillas, A.; Bosch, S.; Markovich, G.; Kahr, B., Relation between 2d/3d Chirality and the Appearance of Chiroptical Effects in Real Nanostructures. *Opt. Express* **2016,** *24*, 2242-2252.

49. Lee, K. S.; El-Sayed, M. A., Dependence of the Enhanced Optical Scattering Efficiency Relative to That of Absorption for Gold Metal Nanorods on Aspect Ratio, Size, End-Cap Shape, and Medium Refractive Index. *J. Phys. Chem. B* **2005,** *109*, 20331-20338.

50. Lee, K. S.; El-Sayed, M. A., Gold and Silver Nanoparticles in Sensing and Imaging: Sensitivity of Plasmon Response to Size, Shape, and Metal Composition. *J. Phys. Chem. B* **2006,** *110*, 19220-19225.

51. Chen, H. J.; Kou, X. S.; Yang, Z.; Ni, W. H.; Wang, J. F., Shape- and Size-Dependent Refractive Index Sensitivity of Gold Nanoparticles. *Langmuir* **2008,** *24*, 5233-5237.

52. Jain, P. K.; Eustis, S.; El-Sayed, M. A., Plasmon Coupling in Nanorod Assemblies: Optical Absorption, Discrete Dipole Approximation Simulation, and Exciton-Coupling Model. *J. Phys. Chem. B* **2006,** *110*, 18243-18253.

53. Tabor, C.; Van Haute, D.; El-Sayed, M. A., Effect of Orientation on Plasmonic Coupling between Gold Nanorods. *ACS Nano* **2009,** *3*, 3670-3678.

54. Shao, L.; Woo, K. C.; Chen, H. J.; Jin, Z.; Wang, J. F.; Lin, H. Q., Angle- and Energy-Resolved Plasmon Coupling in Gold Nanorod Dimers. *ACS Nano* **2010,** *4*, 3053-3062.

55. Lu, X.; Wu, J.; Zhu, Q.; Zhao, J.; Wang, Q.; Zhan, L.; Ni, W., Circular Dichroism from Single Plasmonic Nanostructures with Extrinsic Chirality. *Nanoscale* **2014,** *6*, 14244-14253.

56. Funston, A. M.; Novo, C.; Davis, T. J.; Mulvaney, P., Plasmon Coupling of Gold Nanorods at Short Distances and in Different Geometries. *Nano Lett.* **2009,** *9*, 1651-1658.

57. Su, K. H.; Wei, Q. H.; Zhang, X.; Mock, J. J.; Smith, D. R.; Schultz, S., Interparticle Coupling Effects on Plasmon Resonances of Nanogold Particles. *Nano Lett.* **2003,** *3*, 1087-1090.

58. Plum, E.; Fedotov, V. A.; Zheludev, N. I., Extrinsic Electromagnetic Chirality in Metamaterials. *J. Opt. A: Pure Appl. Opt.* **2009,** *11*, 074009.

59. Rodger, A.; Nordén, B., *Circular Dichroism and Linear Dichroism*. Oxford University Press: Oxford, UK, 1997.

60. Kelly, C.; Tullius, R.; Lapthorn, A. J.; Gadegaard, N.; Cooke, G.; Barron, L. D.; Karimullah, A. S.; Rotello, V. M.; Kadodwala, M., Chiral Plasmonic Fields Probe Structural Order of Biointerfaces. *J. Am. Chem. Soc.* **2018,** *140*, 8509-8517.

61. Furumaki, S.; Yabiku, Y.; Habuchi, S.; Tsukatani, Y.; Bryant, D. A.; Vacha, M., Circular Dichroism Measured on Single Chlorosomal Light-Harvesting Complexes of Green Photosynthetic Bacteria. *J. Phys. Chem. Lett.* **2012,** *3*, 3545-3549.

TOC Graphic:

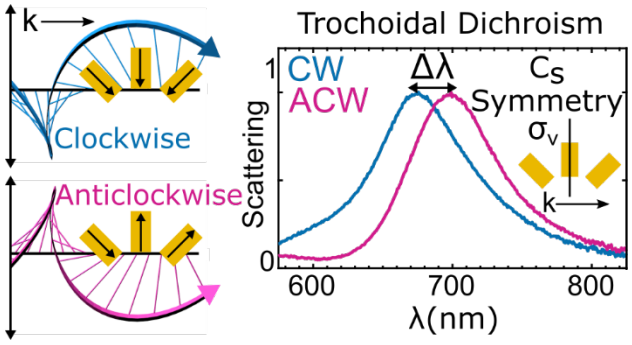
k
Clockwise
Anticlockwise
Trochoidal Dichroism
CW
ACW
Δλ
Cs
Symmetry
σv
k
Scattering
1
0
600
700
800
λ(nm)